Negative magnetization of $Li_2Ni_2Mo_3O_{12}$: A spin system composed of distorted honeycomb lattices and linear chains

Masashi Hase,[1,*] Vladimir Yu. Pomjakushin,[2] Vadim Sikolenko,[3] Lukas Keller,[2] Hubertus Luetkens,[4] Andreas Dönni,[1] and Hideaki Kitazawa[1]

[1]*National Institute for Materials Science, 1-2-1 Sengen, Tsukuba, Ibaraki 305-0047, Japan*
[2]*Laboratory for Neutron Scattering, Paul Scherrer Institut, CH-5232 Villigen PSI, Switzerland*
[3]*Karlsruhe Institute of Technology, Kaiserstrasse 12, D-76131 Karlsruhe, Germany*
[4]*Laboratory for Muon-Spin Spectroscopy, Paul Scherrer Institut, CH-5232 Villigen PSI, Switzerland*

(Received 31 May 2011; revised manuscript received 12 August 2011; published 1 September 2011)

We study the magnetism of a spin-1 substance $Li_2Ni_2Mo_3O_{12}$. The spin system consists of distorted honeycomb lattices and linear chains of Ni^{2+} spins. Li^+ ions enter about 25% and 50% of the honeycomb and chain Ni sites, respectively, creating disorder in both spin subsystems. A magnetic phase transition occurs at $T_c = 8.0$ K in the zero magnetic field. In low magnetic fields, the magnetization increases rapidly below T_c, decreases below 7 K, and finally becomes negative at low temperatures. We determine the magnetic structure using neutron-powder-diffraction results. The honeycomb lattices and linear chains show antiferromagnetic and ferromagnetic long-range order, respectively. We investigate static and dynamic magnetic properties using the local probe technique of muon spin relaxation. We discuss the origin of the negative magnetization.

DOI: 10.1103/PhysRevB.84.104402 PACS number(s): 75.25.−j, 75.30.Cr, 75.40.Cx, 75.47.Lx

I. INTRODUCTION

Several antiferromagnets having plural magnetic ions or magnetic-ion sites show an interesting magnetic long-range order (LRO). In $Cu_2Fe_2Ge_4mO_{13}$, Cu^{2+} spin dimers (spin 1/2) are coupled to Fe^{3+} spin chains (spin 5/2).[1,2] An indirect Fe-Fe exchange coupling via Cu dimers is observed.[3] This result reveals that the Cu dimers play the role of nonmagnetic media in the indirect magnetic interaction. The dynamics of dimer excitation in staggered and random fields generated by Fe spins are also identified experimentally.[4] In $Cu_3Mo_2O_9$, three crystallographically independent Cu^{2+} sites exist (Cu1, Cu2, and Cu3). Spins (1/2) on Cu1 sites form antiferromagnetic (AFM) chains.[5] Two spins on neighboring Cu2 and Cu3 sites form an AFM dimer. Each AFM chain is coupled to AFM dimers. Only a component parallel to the b axis of magnetic moments on Cu1 sites is ordered below the AFM transition temperature $T_N = 7.9$ K in the zero magnetic field.[5] Perpendicular components are ordered in magnetic fields parallel to the a or c axis. A canted AFM LRO is stabilized only in finite magnetic fields. It is inferred that magnetic competition causes this unique LRO. In addition, the canted AFM LRO disappears in $Cu_3Mo_2O_9$ with a very small amount of doping (e.g., 0.2% Zn for Cu sites).[6]

Negative magnetization is an interesting phenomenon. It was observed in $Li_{0.5}(FeCr)_{2.5}O_4$ spinels[7] and explained using the Néel model.[8] In this model, two collinear sublattice magnetizations M_A and M_B with different temperature T dependencies are considered. $|M_A|$ is larger than $|M_B|$ below T_N, while $|M_B|$ is larger than $|M_A|$ below a compensation temperature T_{comp}. If the directions of the sublattice magnetizations are fixed, the magnetization is observed as a negative value below T_{comp}. Several compounds showing a negative magnetization have been found. Some of them are considered to be explainable by the Néel model,[9–18] while for the other compounds the origin is different or has not been determined explicitly.[19–37] Details of the origins will be described later.

Here we turn our attention to $Li_2Ni_2Mo_3O_{12}$. Two crystallographically independent Ni^{2+} (spin 1) sites ($M1$ and $M2$) exist as represented in Fig. 1.[38] The $M1$ and $M2$ sites form distorted honeycomb lattices and linear chains, respectively. About 25% of the $M1$ sites and about 50% of the $M2$ sites are occupied by nonmagnetic Li^+ ions as shown by the formula $Li(Li_{0.5}Ni_{1.5})(Li_{0.5}Ni_{0.5})Mo_3O_{12}$. Unexpectedly, we found negative magnetization at low T. To investigate the origin of the negative magnetization, we determined the magnetic structure of $Li_2Ni_2Mo_3O_{12}$ using the neutron-powder-diffraction technique and its static and dynamic magnetic properties using the local probe technique of muon spin relaxation (μSR).

II. EXPERIMENT

Crystalline powder of $Li_2Ni_2Mo_3O_{12}$ was synthesized using a solid-state-reaction method at 973 K in air for 144 h with intermediate grindings. We used an isotope ^7Li (purity: 99%) for neutron-diffraction samples to decrease the absorption of neutrons. We confirmed the formation of $Li_2Ni_2Mo_3O_{12}$ using an x-ray diffractometer (JDX-3500; JEOL). $Li_2Ni_2Mo_3O_{12}$ is insulating at room temperature.

We measured magnetization using a superconducting quantum interference device magnetometer (MPMS-5S; Quantum Design). We entered powder in paraffin molten by heating in the zero magnetic field and finally fixed the powder in solid paraffin. We measured the magnetization of the powder embedded in solid paraffin. It is likely that the powder directions are randomly distributed and powder reorientation does not occur in the magnetization measurements. The specific heat was measured using a relaxation technique with the Physical Property Measurement System (Quantum Design). We used a sintered pellet in the specific-heat measurements.

We determined the magnetic structure of $^7Li_2Ni_2Mo_3O_{12}$ from neutron-powder-diffraction data. The experiments were conducted using the high-resolution powder diffractometer

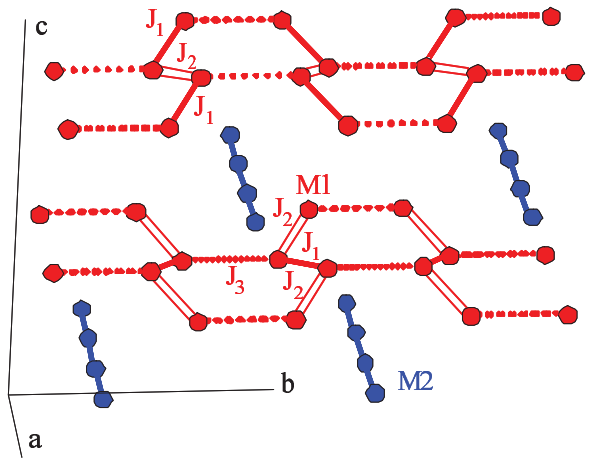

FIG. 1. (Color online) Schematic drawing of $M1$ ($8d$) and $M2$ ($4c$) sites in $Li_2Ni_2Mo_3O_{12}$. The space group is orthorhombic $Pnma$ (No. 62).[38] These sites are occupied by Ni^{2+} (spin-1) or Li^+ (spin-0) ions. The occupation ratio of Ni^{2+} ions is 0.757 at $M1$ and 0.566 at $M2$. The ratio between Ni numbers at $M1$ and $M2$ sites is 0.728:0.272. Three short $M1$-$M1$ bonds exist and form distorted honeycomb lattices. The $M1$-$M1$ distances are 3.03, 3.08, and 3.75 Å at 10 K for the first, second, and third shortest $M1$-$M1$ bonds, respectively. The respective exchange interaction parameters are defined as J_1, J_2, and J_3. The shortest $M2$-$M2$ bonds form linear chains. The $M2$-$M2$ distance is 2.53 Å. Distances in the other Mi-Mi bonds ($i = 1$ or 2) are larger than 5.06 Å. Distances in $M1$-$M2$ bonds are larger than 5.19 Å.

for thermal neutrons[39] (HRPT) (wavelength $\lambda = 1.886$ Å) and the high-intensity cold neutron powder diffractometer DMC ($\lambda = 4.206$ Å) at the Swiss spallation neutron source (SINQ) at Paul Scherrer Institut (PSI). Powder was filled into a vanadium container 8 mm in diameter and 55 mm high. Rietveld refinements of diffraction data were performed using the FULLPROOF SUITE program package.[40] Symmetry analyses of possible magnetic configurations were conducted using the program BASIREP in the FULLPROF SUITE program package.

The μSR measurements were performed using the Dolly spectrometer at the πE1 beamline at the Swiss Muon Source at PSI. In a μSR experiment nearly 100% spin-polarized muons are implanted into the sample one at a time. The positively charged μ^+ thermalize at interstitial lattice sites, where they act as magnetic microprobes. In a magnetic material the muon spin precesses about the local magnetic field B at the muon site with the Larmor frequency $f_\mu = \gamma_\mu/2\pi\, B$ (muon gyromagnetic ratio $\gamma_\mu/2\pi = 135.5\,\mathrm{MHz\,T^{-1}}$). With a lifetime of $\tau_\mu = 2.2\,\mu$s, the muon decays into two neutrinos and a positron, the latter being predominantly emitted in the direction of the muon spin at the moment of the decay. The measurement of both the direction of positron emission and the time between muon implantation and positron detection for an ensemble of hundreds of thousands of muons provides the time evolution of the muon spin polarization $P(t)$ in the initial muon spin direction. In a powder, two-thirds of the local magnetic-field components are perpendicular to the μ^+ spin and cause a precession, while the one-third of longitudinal field components do not. The damping of the oscillation is a measure of the width of the static field distribution experienced by the muon ensemble. In a static magnetic environment, one-third of the muon spin polarization is conserved. In a dynamic magnetic material, however, this so-called one-third tail also relaxes and in certain limits the relaxation rate can be related to magnetic fluctuation rates. Since μSR is a local probe technique, the amplitudes of the different signals observed are a measure of the corresponding volume fractions. With this, it provides a direct measure of magnetic volumes, which is not easily possible with scattering techniques. For further details of the μSR technique, we refer the reader to the recent review in Ref. 41.

III. RESULTS

Figure 2 portrays the T dependence of the specific heat in the zero magnetic field. A peak is apparent at 8.0 K. As will be shown later, magnetization increases rapidly on cooling below 8.0 K. Therefore, the peak indicates the occurrence of a magnetic phase transition at $T_c = 8.0$ K.

Figure 3(a) shows the T dependence of the magnetization M of $Li_2Ni_2Mo_3O_{12}$ in a very weak residual magnetic field. The value of the magnetic field was estimated as 6.3×10^{-5} T (0.63 Oe) from paramagnetic magnetization values in this field and 0.1 T. The magnetization increases rapidly below 8.2 K, shows a maximum around 7.2 K, and decreases below 7.2 K. It should be noted that the magnetization is negative below 4.2 K. We did not observe any difference between magnetizations measured for increasing and decreasing T. Figure 4 represents the magnetic-field H dependence of M at 1.7 K after the residual field cooling process. We can see a small residual magnetization and hysteresis. The rapid increase below 8.2 K and small residual magnetization indicate the appearance of a canted AFM LRO or ferromagnetic (FM) LRO with small magnetic moments. Figure 3(b) shows the T dependence of M in the field of 1×10^{-3} T. We can see a hysteresis between magnetizations measured in the residual field cooling (RFC) and field cooling (FC) processes. The absolute value of M in the FC process is larger than that in the RFC process. In 0.1 T [Fig. 3(d)], only the FC magnetization becomes negative. In 0.2 T [Fig. 3(e)], both the RFC and FC magnetizations are positive. In 1 T [Fig. 3(f)], the hysteresis is small. Figure 3(g) shows the T dependence of paramagnetic susceptibility in 0.1 T. The susceptibility above 20 K obeys the Curie-Weiss law. We determined the value of the Curie constant as 1.12 emu K/mol Ni from the data above 200 K. The g value

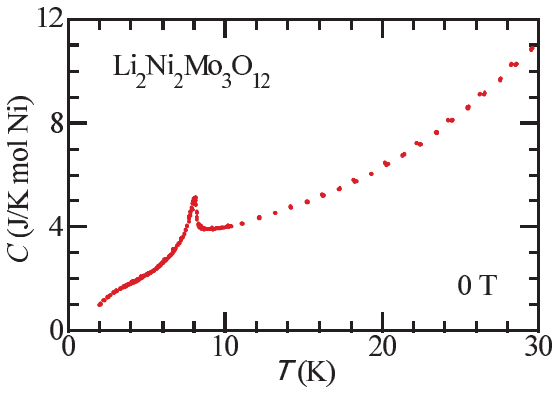

FIG. 2. (Color online) Temperature dependence of the specific heat of $Li_2Ni_2Mo_3O_{12}$ in the zero magnetic field.

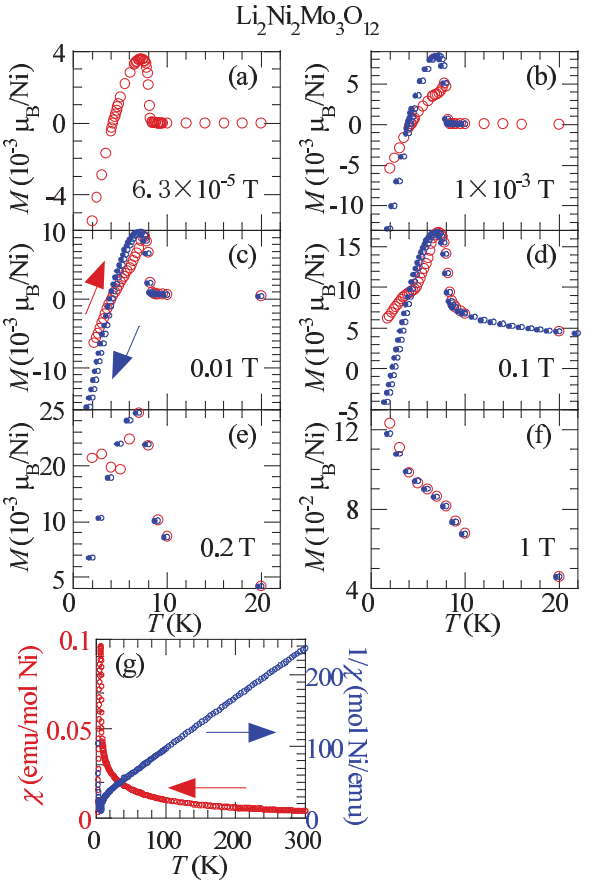

FIG. 3. (Color online) (a)–(f) Temperature dependence of the magnetization of $Li_2Ni_2Mo_3O_{12}$ at low T in various magnetic fields. Open and closed circles indicate data measured in the RFC and FC processes, respectively. (g) Temperature dependence of the magnetic susceptibility and its inverse in the paramagnetic state.

was calculated as 2.11 on the assumption that the spin value is 1. This g value is reasonable for Ni^{2+} spins.

Figure 5 depicts the neutron-powder-diffraction pattern of paramagnetic $^7Li_2Ni_2Mo_3O_{12}$ recorded using the HRPT diffractometer with $\lambda = 1.886$ Å at 10 K, which is slightly higher than $T_c = 8.0$ K. The refinement based on the crystal structure of $Li_2Ni_2Mo_3O_{12}$ as determined by room-temperature single-crystal x-ray diffraction[38] fits the experimental neutron-diffraction pattern at 10 K well. Structural parameters are presented in Table I.

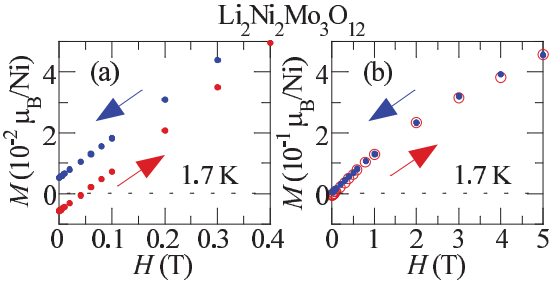

FIG. 4. (Color online) Magnetic-field dependence of the magnetization of $Li_2Ni_2Mo_3O_{12}$ at 1.7 K. Arrows indicate the directions of the magnetic-field scans.

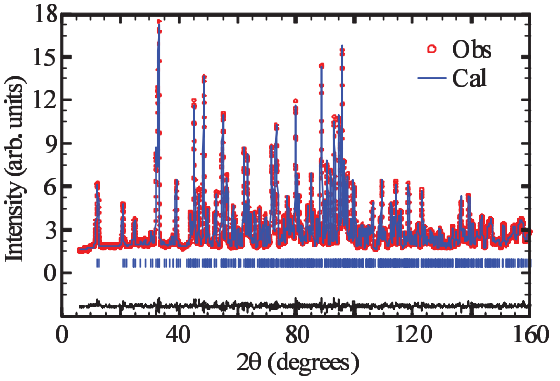

FIG. 5. (Color online) Neutron-powder-diffraction pattern of $^7Li_2Ni_2Mo_3O_{12}$ at 10 K (higher than T_c) measured using the HRPT diffractometer ($\lambda = 1.886$ Å). Lines on the observed pattern and at the bottom show a Rietveld refined pattern and the difference between the observed and the Rietveld refined patterns. Hash marks represent the positions of nuclear reflections.

Figure 6(a) shows the difference between two neutron-powder-diffraction patterns of $^7Li_2Ni_2Mo_3O_{12}$ at 2.0 and 10 K collected using the DMC diffractometer ($\lambda = 4.206$ Å). The reflections of the difference pattern can be indexed in the chemical cell with the propagation vector $\mathbf{k} = \mathbf{0}$. The profile matching Le Bail fit, in which the integral intensities are the refined parameters, shows that all the peaks are well described with $\mathbf{k} = \mathbf{0}$ with the reliability factors $R_{wp} = 2.34$, $R_{\rm exp} = 1.72$, and $\chi^2 = 1.86$. The new reflections appear below T_c; therefore, they must be magnetic reflections.

Using the determined propagation vector, we performed a symmetry analysis according to Izyumov *et al.*[42] to derive possible magnetic configurations for the space group $Pnma$. The space group has eight one-dimensional irreducible representations (IRs). The observed magnetic patterns were compared with calculated patterns using the structural parameters determined from the structural refinement. After sorting out the basis functions of all eight IRs, we found that only τ_5 fits the experimental pattern well. The IR τ_5 has the characters 1, −1, 1, −1, 1, −1, 1, −1 for the symmetry elements listed in the caption of Fig. 7. The magnetic moments of Ni2 atoms are restricted by τ_5 symmetry to be parallel to the b axis, thus forming a ferromagnetic sublattice. The y components of Ni1 spins are also forced to be ferromagnetically aligned, whereas the spins in xz plane have an antiferromagnetic configuration with the basis vectors listed in the caption of Fig. 7.

In the refinement of the magnetic structure, all the atom structure parameters were fixed by the values obtained from HRPT data (Table I). The magnetic structure is depicted in Fig. 7. The magnetic moment at the Ni1(1) position is [0.27(4), 0.04(12), −1.58(3)]μ_B/Ni and its magnitude is 1.60(3)μ_B/Ni at 2.0 K. The ordered Ni1 moment mainly points in the c direction with a small component in the a direction. The size of the ferromagnetic b component is refined to a small value close to zero within experimental error bars. The arrangement of the moments indicates that the J_1, J_2, and J_3 interactions are FM, FM, and AFM, respectively. The magnetic moment at the Ni2(1) position is [0, −0.6(1), 0]μ_B/Ni. Ni2 moments form the FM LRO. The Ni2 moment is reduced in comparison with ordinary ordered Ni^{2+} moments. The reduction may be

TABLE I. Structural parameters of $^7Li_2Ni_2Mo_3O_{12}$ derived from Rietveld refinement of the HRPT neutron-powder-diffraction pattern at 10 K. The space group is orthorhombic *Pnma* (No. 62). The lattice constants at 10 K are $a = 5.0639(5)$ Å, $b = 10.397(1)$ Å, and $c = 17.467(2)$ Å. Estimated standard deviations are shown in parentheses. The atomic displacement parameters B_{iso} were constrained to be the same for the same atom types and for the atoms occupying the same site. The reliability factors of the refinement amounted to $R_{wp} = 3.21$, $R_{exp} = 1.77$, $\chi^2 = 3.31$, and $R_{Bragg} = 2.76$

Atom	Site	x	y	z	B_{iso} (Å^2)	Occupancy
Ni1	8*d*	0.7473(3)	0.4302(1)	0.0258(1)	0.27(3)	0.757(2)
Li1	8*d*	0.7473(3)	0.4302(1)	0.0258(1)	0.27(3)	0.243(2)
Ni2	4*c*	0.3881(6)	0.75	0.2497(2)	0.27(3)	0.566(2)
Li2	4*c*	0.3881(6)	0.75	0.2497(2)	0.27(3)	0.434(2)
Li3	4*c*	0.7562(13)	0.25	0.1967(3)	0.27(3)	
Mo1	4*c*	0.7149(4)	0.75	0.0562(1)	0.06(2)	
Mo2	8*d*	0.2225(3)	0.4739(1)	0.1562(1)	0.06(2)	
O1	4*c*	0.5657(5)	0.25	0.0064(1)	0.29(2)	
O2	4*c*	0.6353(5)	0.75	0.1544(1)	0.29(2)	
O3	8*d*	0.1383(4)	0.6184(2)	0.2050(1)	0.29(2)	
O4	8*d*	0.4233(4)	0.3779(2)	0.2137(1)	0.29(2)	
O5	8*d*	0.9411(4)	0.3864(2)	0.1256(1)	0.29(2)	
O6	8*d*	0.4214(4)	0.5122(2)	0.0740(1)	0.29(2)	
O7	8*d*	0.9163(4)	0.6146(2)	0.0363(1)	0.29(2)	

caused by the one dimensionality of the Ni2 spin system and large disorder due to about 50% substitution of Li ions.

The IR τ_5 fits the experimental data well for all the measured temperatures. Figure 8 shows the T dependence of the magnetic moments. The absolute value of the FM component m_{2b} increases monotonically with decreasing T. The AFM components m_{1a} and m_{1c} have a significantly weaker dependence of temperature with steplike change at T_c. The FM component m_{1b} stays close to zero with a slight tendency to increase.

To further elucidate the static and dynamic magnetic properties of $Li_2Ni_2Mo_3O_{12}$, we performed zero-field μSR experiments for various temperatures. In Fig. 9 zero-field μSR spectra are shown for characteristic temperatures above and below $T_c = 8.0$ K. Figures 9(a) and 9(b) show the same data but plotted on different time scales to highlight the observed changes for the fast and slow relaxing signals. At high temperatures a slowly relaxing spectrum of Gauss-Kubo-Toyabe form[43] is observed. This is the distinctive identifying characteristic of a nonmagnetic material. The small Gaussian relaxation σ_{nm} is due to static random nuclear moments only. Below $T_c = 8.0$ K an overdamped spontaneous muon spin precession is observed, indicating a very broad field distribution at the muon site(s), i.e., a complicated or disordered magnetic structure or many muon sites in the crystallographic lattice. This result is consistent with structural disorder caused by Li ions.

The μSR spectra have been fitted using the following functional form for the polarization function:

$$P(t) = (1 - f_{mag})\, G_{nm}(t) + f_{mag}\, G_{mag}(t) \qquad (1)$$

with

$$G_{nm}(t) = \left(\tfrac{2}{3}[1 - (\sigma_{nm}t)^2]e^{-(\sigma_{nm}t)^2/2} + \tfrac{1}{3}\right)e^{-\lambda_{dyn}t} \qquad (2)$$

and

$$G_{mag}(t) = \left(\tfrac{2}{3}\cos(2\pi f_\mu t)e^{-(\sigma_{mag}t)^2/2} + \tfrac{1}{3}\right)e^{-\sqrt{\lambda_{dyn}t}}. \qquad (3)$$

Here G_{mag} and G_{nm} represent the relaxation functions for the magnetic f_{mag} and nonmagnetic $1 - f_{mag}$ volume fractions with their corresponding relaxation rates σ_{mag} and σ_{nm}, respectively, and λ_{dyn} is the dynamic relaxation rate.

Figure 10 shows the parameter values obtained from the fits using the preceding equations. A sharp magnetic transition at $T_c = 8.0$ K is observed in all the parameters. The magnetic fraction f_{mag} reaches ≈100% shortly below T_c. The magnetic order parameter measured via the μSR frequency f_μ and the static field width σ_{mag} continuously increase below T_c. The values of σ_{mag} are larger than the values of f_μ, indicating the very broad width of the internal field distribution. Approaching the transition from above, an additional exponential damping that increases toward T_c is observed. This is typical for the slowing down of electronic moments approaching T_c. The corresponding dynamic relaxation rate λ_{dyn} is shown in Fig. 10(d). Below the transition λ_{dyn} is nearly zero, indicating a static magnetic state. Decreasing the temperature further, a dynamic relaxation of the one-third tail is observed again. This is already clearly visibly from the comparison of the μSR spectra at 7.6 and 1.9 K in Fig. 9(b). The dynamic relaxation at low temperature had to be fitted with a root-exponential time dependence [Eq. (3)], which is indicative of a broad distribution of fluctuation times. Interestingly, the dynamic relaxation rate starts to increase below ≈4 K where the magnetization becomes negative.

IV. DISCUSSION

Let us consider the origin of the negative magnetization in $Li_2Ni_2Mo_3O_{12}$. The Néel model requires two FM sublattices, which in our case are formed by the m_{1b} and m_{2b} components.

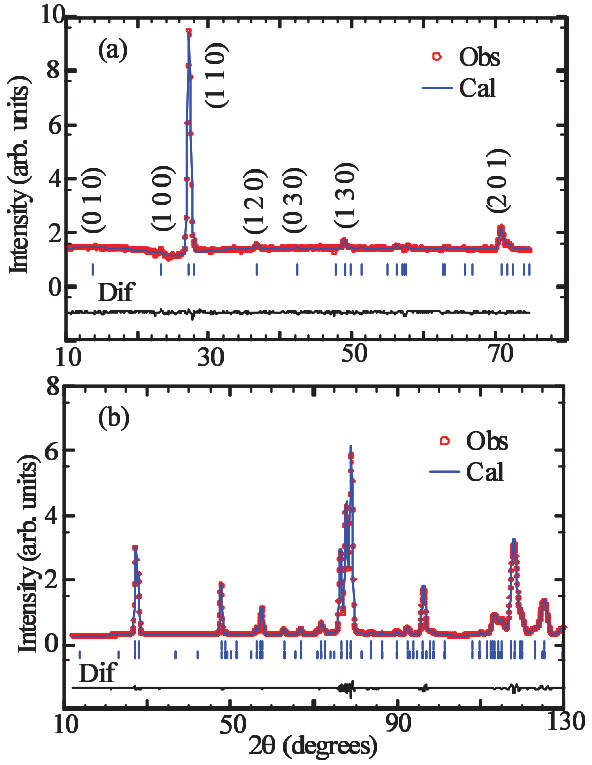

FIG. 6. (Color online) (a) Fragment of the difference between two neutron-powder-diffraction patterns of $^7Li_2Ni_2Mo_3O_{12}$ at 2.0 and 10 K (magnetic neutron-diffraction pattern) measured using the DMC diffractometer ($\lambda = 4.206$ Å). Lines on the observed pattern and at the bottom show a Rietveld refined pattern in the Le Bail profile matching mode and the difference between the observed and the Rietveld refined patterns. Hash marks represent positions of magnetic reflections. Several indices of the reflections are written. (b) Neutron-powder-diffraction pattern at 2.0 K. Lines on the observed pattern and at the bottom show a Rietveld refined pattern for the magnetic structure model τ_5 and the difference between the observed and the Rietveld refined patterns. Upper and lower hash marks represent the positions of nuclear and magnetic reflections, respectively.

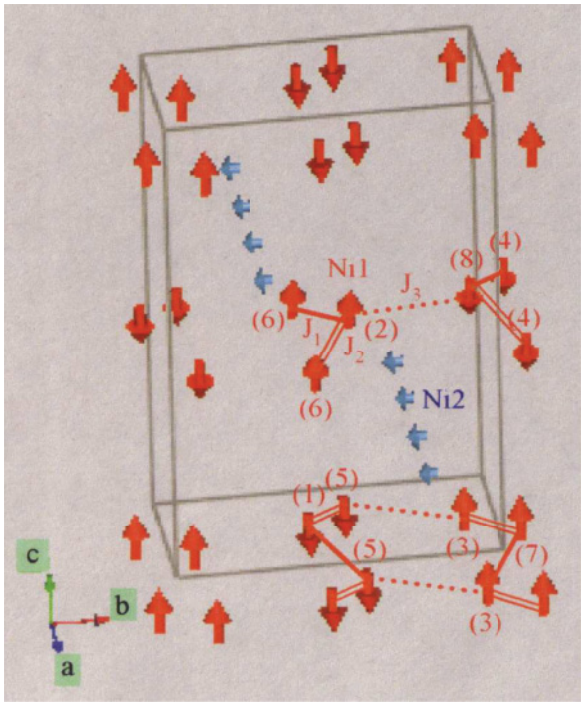

FIG. 7. (Color online) Magnetic structure of $Li_2Ni_2Mo_3O_{12}$. Ni2 moments form a FM LRO. To show the arrangement of Ni1 moments clearly, the symmetry operators of $M1$ ($8d$) sites are given: (1) $x,y,z[u,v,w]$; (2) $\bar{x}+1/2,\bar{y},z+1/2[u,v,\bar{w}]$; (3) $\bar{x},y+1/2,\bar{z}[\bar{u},v,\bar{w}]$; (4) $x+1/2,\bar{y}+1/2,\bar{z}+1/2[\bar{u},v,w]$' (5) $\bar{x},\bar{y},\bar{z}[u,v,w]$; (6) $x+1/2,y,\bar{z}+1/2[u,v,\bar{w}]$; (7) $x,\bar{y}+1/2,z[\bar{u},v,\bar{w}]$; and (8) $\bar{x}+1/2,y+1/2,z+1/2[\bar{u},v,w]$. Here u, v, and w indicate components of the magnetic moment.

The values of m_{2b} are negative. The values of m_{1b} are very small and show both signs. At 2.0 K, the error bar of m_{1b} is the smallest and the value of m_{1b} is positive. Therefore, if the T dependence of m_{1b} is similar to that of $-m_{1c}$ or m_{1a}, m_{1b} may be intrinsically positive. Compensation of m_{1b} and m_{2b} is possible. The sublattice magnetizations M_A and M_B defined in Sec. I correspond to m_{1b} and m_{2b}, respectively. M_A has a weaker T dependence than M_B in the Néel model. If m_{1b} is proportional to $-m_{1c}$ or m_{1a}, m_{1b} has a weaker T dependence than m_{2b}, as in the Néel model. We calculated the average spontaneous magnetization per Ni $m_s = p_1 m_{1b} + (1 - p_1)m_{2b}$ and plotted it together with the RFC magnetization in Fig. 8(c). Here the proportion coefficient $p_1 = 0.728$ is calculated from the occupancies listed in Table I. The contribution of m_{1b} is large in m_s because of the large number of Ni1 atoms. Although the component m_{2b} shows a well-defined decrease with decreasing temperature [Fig. 8(b)], m_s is practically constant [Fig. 8(c)]. The difference in the T dependence of m_{2b} and m_s suggests compensation of the FM components. A reversal of m_s, however, was not obtained. The absolute values of m_s seem much larger than the absolute values of the RFC magnetization represented by the solid line in Fig. 8(c).

The negative magnetization is too small to be detected using neutron-powder-diffraction techniques. Therefore, we could not verify the validity of the Néel model. The magnetic scattering length was calculated as $2.7gSf(Q)$ fm using a Born approximation. Here g and S are the g value and magnitude of ordered spins, respectively, and $f(Q)$ is the magnetic form factor whose magnitude is on the order of unity or less. The nuclear coherent scattering length of Ni was obtained as 10.3 fm (natural average).[44] The intensity of the Bragg peaks is proportional to the square of the scattering lengths. The lower limit of magnetic moments that can be evaluated in neutron-powder-diffraction experiments is about $0.1\mu_B$. As shown in Fig. 8, the error bars are on the order of $0.1\mu_B$.

The following four alternative models may be considered as possible explanations of the negative magnetization effect. In model 1 applicable to $GdCrO_3$ or $(LaX_{RE})CrO_3$ (X_{RE} = Pr or Nd),[19–24] magnetic moments of Cr ions form a canted AFM LRO, while rare-earth (RE) ions are paramagnetic. A Dzyaloshinskii-Moriya (DM) interaction exists between Cr and X_{RE} spins. The main component x of the Cr moment produces an internal magnetic field parallel to the z direction on RE ions. The polarization of paramagnetic moments on RE ions induced by the internal magnetic field is aligned opposite the canted components parallel to the z direction.

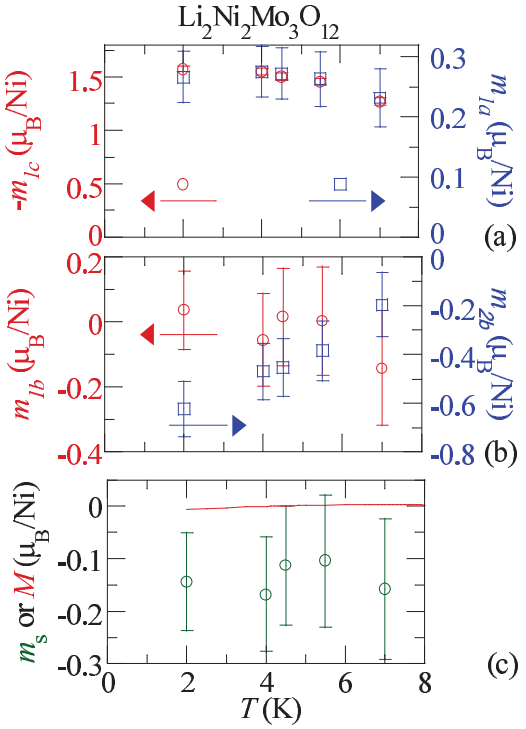

FIG. 8. (Color online) Temperature dependence of the components of ordered magnetic moments in $Li_2Ni_2Mo_3O_{12}$: (a) $-m_{1c}$ and m_{1a} and (b) m_{1b} and m_{2b}. (c) Average spontaneous magnetization per Ni m_s. The solid line represents the RFC magnetization shown in Fig. 3(a).

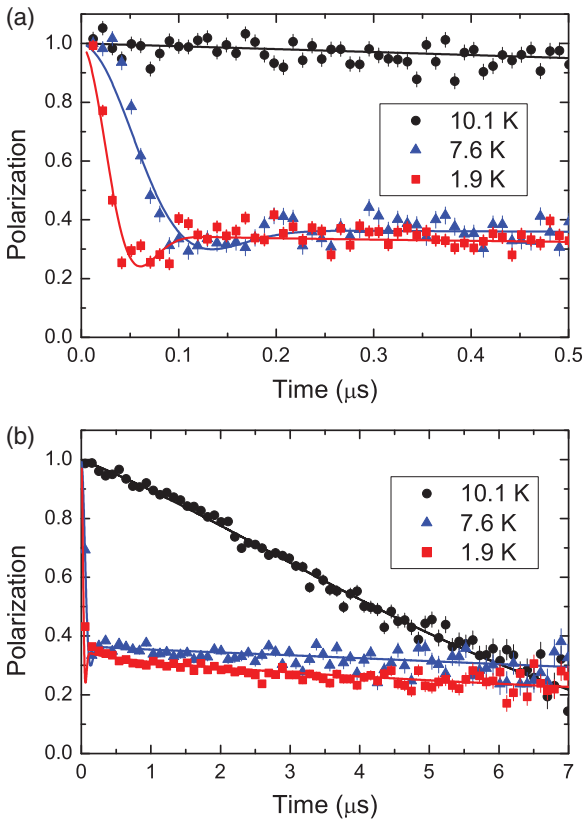

FIG. 9. (Color online) Zero-field muon spin relaxation spectra for various characteristic temperatures shown on (a) a short- or (b) a long-time scale.

The magnitude of the sum of the canted components is larger than the magnitude of the sum of the polarization of the paramagnetic magnetization below T_N, while the latter becomes larger than the former below T_{comp}. The direction of the main component of the Cr moments is fixed. Therefore, the direction of the canted component is also fixed. As a result, the negative magnetization appears in $GdCrO_3$ or $(LaX_{RE})CrO_3$ (X_{RE} = Pr or Nd). In $Li_2Ni_2Mo_3O_{12}$, the distance between Ni1 and Ni2 sites is larger than 5.19 Å. Exchange interactions between Ni1 and Ni2 spins are probably weak. Internal magnetic fields produced by Ni1 (Ni2) moments on Ni2 (Ni1) sites are small. Accordingly, the negative magnetization in $Li_2Ni_2Mo_3O_{12}$ cannot be explained by model 1.

In model 2, which is applicable to $LaVO_3$ (Refs. 26–28) or YVO_3,[29–31] only the canted component of the magnetic moment on V ions reverses and becomes antiparallel to external fields. Therefore, negative magnetization was observed. In $LaVO_3$, a structural phase transition occurs just below T_N due to the Jahn-Teller effect. As a result, the DM vector reverses and therefore the canted component of the magnetic moment reverses. In YVO_3, the canting direction is determined mainly by the single-ion anisotropy at high T and by the DM interaction at low T. As a result, the canting direction reverses at low T. In $Li_2Ni_2Mo_3O_{12}$, the LRO of Ni2 spins is the FM order (not the canted AFM order). Consequently, model 2 cannot account for the negative magnetization in $Li_2Ni_2Mo_3O_{12}$.

In model 3, which is applicable to $(SmGd)Al_2$,[32] compensation between the spin and the orbital parts of the ordered moments occurs. We observe a sum of spin and orbital magnetic moments. Therefore, the results in Fig. 8 indicate directly that compensation between the spin and the orbital parts of the ordered moments is not the origin of the negative magnetization. In addition, in 3*d* shells, only spin magnetic moments exist because of quenching of the orbital angular momentum.

In model 4, which is possibly applicable to $Sr_2X_{RE}RuO_6$ (X_{RE} = Yb, Y, or Lu),[33–36] exchange bias (EB) effects[45] may cause negative magnetization. The effects can appear in composites having both FM and AFM LROs. Ordered magnetic moments of the two LROs should be collinear. The FM transition temperature should be higher than the AFM transition temperature. In $Li_2Ni_2Mo_3O_{12}$, however, Ni1 and Ni2 moments are nearly perpendicular to each other. Only one transition was observed within experimental accuracy. In addition, the distances between Ni1-Ni2 bonds are larger than 5.19 Å, suggesting that interactions between Ni1 and Ni2 spins are weak. Consequently, EB effects cannot account for the negative magnetization in $Li_2Ni_2Mo_3O_{12}$.

At present, we think that the Néel model may be valid for the negative magnetization in $Li_2Ni_2Mo_3O_{12}$, although we cannot prove the validity of the Néel model. We cannot absolutely deny the possibility of another (unknown) origin. As described by the μSR results, the dynamic relaxation rate starts to increase below $\approx$4 K where the magnetization becomes negative. It is tempting to conclude that the

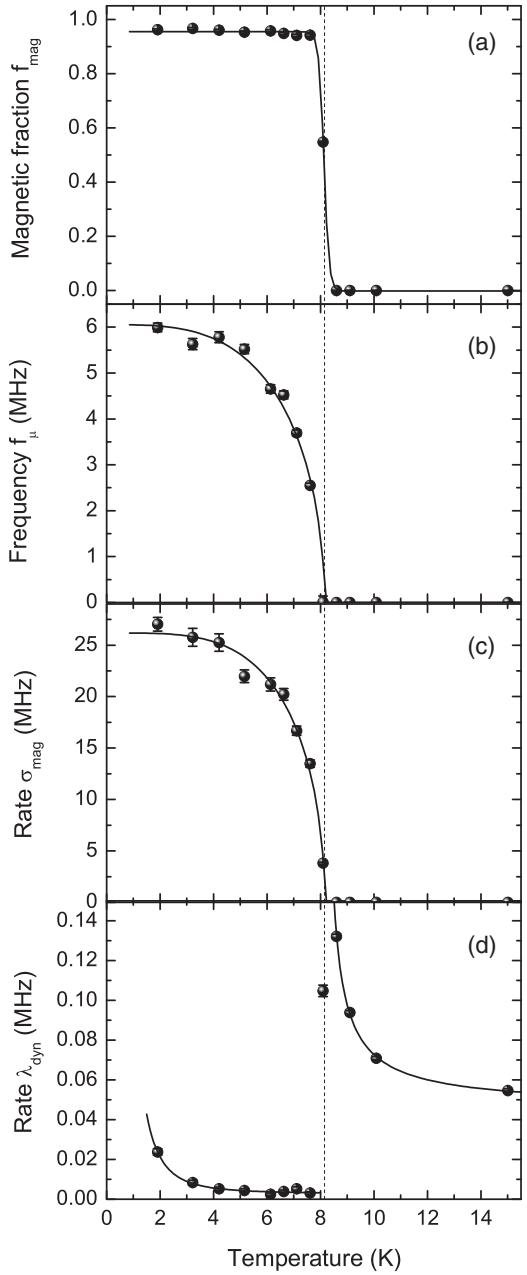

FIG. 10. Parameter values obtained from the fits to the zero-field muon spin relaxation measurements. The lines are guides to the eye.

magnetization inversion mechanism involves a dynamic process. An alternative idea is that an undetected structural change may cause reversal of m_{2b}. Experimental investigations into $Li_2Ni_2Mo_3O_{12}$ using other techniques and further theoretical considerations are necessary.

V. CONCLUSION

We studied the magnetism of the spin-1 substance $Li_2Ni_2Mo_3O_{12}$. The spin system is composed of the distorted honeycomb lattices and linear chains formed by two distinct Ni^{2+} sites, Ni1 and Ni2, respectively. Li^+ ions substitute about 25% and 50% of the honeycomb and chain Ni sites, respectively, creating the disorder in both spin subsystems. A magnetic phase transition occurs at $T_c = 8.0$ K. In low magnetic fields, the magnetization increases rapidly just below T_c, decreases below 7 K, and finally becomes negative at low temperatures on cooling. We determined the magnetic structure using neutron-powder-diffraction results. The magnetic order on both Ni sites develops according to a single irreducible representation τ_5 of the space group $Pnma$ and propagation vector $\mathbf{k} = \mathbf{0}$. The honeycomb lattices show antiferromagnetic long-range order. The ordered Ni1 moment mainly points in the c direction with a small AFM component in the a direction. The size of the ferromagnetic b component is very small. The ordered Ni2 moment on linear chains has only the b component and shows FM long-range order. The magnetic moment sizes amounted to $1.60(3)\mu_B$ and $0.6(1)\mu_B$ per Ni atom for the honeycomb lattice and chain Ni sites, respectively. The sharp magnetic transition at T_c was also observed in the μSR results. The overdamped spontaneous muon spin precession below T_c indicates a very broad field distribution at the muon site(s). The dynamic relaxation rate starts to increase below $\approx$4 K where the magnetization becomes negative. We have examined several models known from literature that can account for the negative magnetization. The Néel model that is based on compensation of the ferromagnetic sublattices may be valid in our case, but our experimental data do not allow us to prove this model quantitatively.

ACKNOWLEDGMENTS

We are grateful to H. Mamiya for fruitful discussion, S. Matsumoto for sample syntheses and x-ray diffraction measurements, and M. Kaise for x-ray diffraction measurements. The neutron-powder-diffraction experiments were conducted at SINQ, PSI Villigen, Switzerland. The μSR measurements were performed at the Swiss Muon Source, PSI Villigen, Switzerland. This work was partially supported by grants from NIMS.

*HASE.Masashi@nims.go.jp

[1]T. Masuda, A. Zheludev, B. Grenier, S. Imai, K. Uchinokura, E. Ressouche, and S. Park, Phys. Rev. Lett. **93**, 077202 (2004).
[2]T. Masuda, A. Zheludev, B. Sales, S. Imai, K. Uchinokura, and S. Park, Phys. Rev. B **72**, 094434 (2005).
[3]T. Masuda, K. Kakurai, M. Matsuda, K. Kaneko, and N. Metoki, Phys. Rev. B **75**, 220401(R) (2007).
[4]T. Masuda, K. Kakurai, and A. Zheludev, Phys. Rev. B **80**, 180412(R) (2009).
[5]T. Hamasaki, T. Ide, H. Kuroe, T. Sekine, M. Hase, I. Tsukada, and T. Sakakibara, Phys. Rev. B **77**, 134419 (2008).
[6]M. Hase, H. Kitazawa K. Ozawa, T. Hamasaki, H. Kuroe, and T. Sekine, J. Phys. Soc. Jpn. **77**, 034706 (2008).
[7]E. W. Gorter and J. A. Schulkes, Phys. Rev. **90**, 487 (1953).

[8]L. Néel, Ann. Phys. (Paris) **3**, 137 (1948).
[9]N. Menyuk, K. Dwight, and D. G. Wickham, Phys. Rev. Lett. **4**, 119 (1960).
[10]K. Yasukochi, K. Kanematsu, and T. Ohoyama, J. Phys. Soc. Jpn. **15**, 932 (1960).
[11]J. A. Schulkes and G. Blasse, J. Phys. Chem. Solids **24**, 1651 (1963).
[12]B. Lüthi, Phys. Rev. **148**, 519 (1966).
[13]M. Abe, M. Kawachi, and S. Nomura, J. Phys. Soc. Jpn. **31**, 940 (1971).
[14]A. K. M. Zakaria and M. A. Asgar, J. Alloys Compd. **396**, 44 (2005).
[15]Y. Kimishima, Y. Ichiyanagi, K. Shimizu, and T. Mizuno, J. Magn. Magn. Mater. **210**, 244 (2000).
[16]Y. Kimishima, M. Uehara, and T. Saitoh, Solid State Commun. **133**, 559 (2005).
[17]V. Yu Ivanov, A. A. Mukhin, A. S. Prokhorov, and A. M. Balbashov, Phys. Status Solidi B **236**, 445 (2003).
[18]S. Hashimoto, Y. Matsuda, T. Sato, and S. Anzai, J. Appl. Phys. **98**, 123903 (2005).
[19]A. H. Cooke, D. M. Martin, and M. R. Wells, J. Phys. C **7**, 3133 (1974).
[20]S. Washimiya and C. Satoko, J. Phys. Soc. Jpn. **45**, 1204 (1978).
[21]K. Yoshii, J. Solid State Chem. **159**, 204 (2001).
[22]K. Yoshii and A. Nakamura, J. Solid State Chem. **155**, 447 (2000).
[23]K. Yoshii, A. Nakamura, Y. Ishii, and Y. Morii, J. Solid State Chem. **162**, 84 (2001).
[24]V. A. Khomchenko, I. O. Troyanchuk, R. Szymczak, and H. Szymczak, J. Mater. Sci. **43**, 5662 (2008).
[25]B. Andrzejewski, A. Kowalczyk, J. E. Frackowiak, T. Toliński, A. Szlaferek, S. Pal, and Ch. Simon, Phys. Status Solidi B **243**, 295 (2006).
[26]N. Shirakawa and M. Ishikawa, Jpn. J. Appl. Phys. **30**, L755 (1991).
[27]A. V. Mahajan, D. C. Johnston, D. R. Torgeson, and F. Borsa, Phys. Rev. B **46**, 10966 (1992).
[28]H. C. Nguyen and J. B. Goodenough, Phys. Rev. B **52**, 324 (1995).
[29]Y. Ren, T. T. M. Palstra, D. I. Khomskii, E. Pellegrin, A. A. Nugroho, A. A. Menovsky, and G. A. Sawatzky, Nature (London) **396**, 441 (1998).
[30]Y. Ren, T. T. M. Palstra, D. I. Khomskii, A. A. Nugroho, A. A. Menovsky, and G. A. Sawatzky, Phys. Rev. B **62**, 6577 (2000).
[31]G. R. Blake, T. T. M. Palstra, Y. Ren, A. A. Nugroho, and A. A. Menovsky, Phys. Rev. B **65**, 174112 (2002).
[32]H. Adachi and H. Ino, Nature (London) **401**, 148 (1999).
[33]R. P. Singh and C. V. Tomy, J. Phys. Condens. Matter **20**, 235209 (2008).
[34]R. P. Singh and C. V. Tomy, Phys. Rev. B **78**, 024432 (2008).
[35]R. P. Singh, C. V. Tomy, and A. K. Grover, Appl. Phys. Lett. **97**, 182505 (2010).
[36]R. P. Singh and C. V. Tomy, Solid State Commun. **150**, 804 (2010).
[37]E. Duman, M. Acet, Y. Elerman, A. Elmali, and E. F. Wassermann, J. Magn. Magn. Mater. **238**, 11 (2002).
[38]M. Ozima, S. Sato, and T. Zoltai, Acta Crystallogr. Sect. B **33**, 2175 (1977).
[39]P. Fischer, G. Frey, M. Koch, M. Koennecke, V. Pomjakushin, J. Schefer, R. Thut, N. Schlumpf, R. Buerge, U. Greuter, S. Bondt, and E. Berruyer, Physica B **276**, 146 (2000); [http://sinq.web.psi.ch/hrpt].
[40]J. Rodríguez-Carvajal, Physica B (Amsterdam) **192**, 55 (1993).
[41]A. Yaouanc and P. Dalmas de Réotier, *Muon Spin Rotation, Relaxation, and Resonance: Applications to Condensed Matter* (Oxford University Press, Oxford, 2011).
[42]Y. A. Izyumov, V. E. Naish, and R. P. Ozerov, *Neutron Diffraction of Magnetic Materials* (Consultants Bureau, New York, 1991).
[43]R. Kubo, Hyperfine Interact. **8**, 731 (1981).
[44]A. Rauch and W. Waschkowski, in *Neutron Data Booklet*, edited by A.-J. Dianoux and G. Lander (Old City, Philadelphia, 2003), Chap. 1.1.
[45]J. Nogués and Ivan K. Schuller, J. Magn. Magn. Mater. **192**, 203 (1999).